Quantum emitter interacting with a *h*-BN layer in the strong-coupling regime

Vasilios Karanikolas *

International Center for Young Scientists (ICYS), National Institute for Materials Science (NIMS) 1-1 Namiki, Tsukuba, Ibaraki 305-0044, Japan

(Received 19 June 2020; revised 2 August 2020; accepted 4 August 2020; published 27 August 2020)

We present that the hexagonal boron nitride (*h*-BN) layer is a platform that facilitates strong light-matter interactions. We calculate the emission spectrum of a quantum emitter (QE) interacting with the *h*-BN layer at the strong-coupling regime. The *h*-BN layer supports phonon polariton modes at the far-infrared part of the spectrum that lead to a 10^4 confinement of light. The phonon polaritons are the main channel of relaxation of the QE, where the Purcell factor of the QE shows an enhancement of the relaxation rate above three orders of magnitude, compared to the free space value, when it is placed 100 nm above the *h*-BN layer. At smaller separation distances of the QE with the *h*-BN layer the total system operates in the strong-coupling regime, which appears as two peaks in the emission spectrum, splitting the single emission peak of the QE emitting in the free space. This energy splitting is the Rabi splitting $\hbar\Omega$ that depends on the transition energy $\hbar\omega_0$ of the QE, the position and the free-space relaxation rate of the QE, reaching values of $\Omega/\omega_0 = 23.5\%$.

DOI: 10.1103/PhysRevB.102.075446

I. INTRODUCTION

The emission properties of a quantum emitter (QE) strongly depend to its environment; its relaxation rate can be engineered by placing the QE in proximity to a specific nanostructure. Usually conducting nanostructures are considered, where the QE relaxes by exciting the surface plasmon modes [1–4], instead of emitting in the far-field. The surface plasmon modes are hybrid modes of the free electrons, provided by the metal, and the electromagnetic (EM) field; these modes are confined perpendicular to the metal-dielectric interface and propagate along it, until the material losses completely dumped them [5]. Noble metals are routinely used as plasmonic materials, where their resonance response is mainly in the visible part of the spectrum and their functionality is limited due to the material losses [6]. Patterned noble metal nanostructures form metamaterials which have optical response in a wider part of the EM spectrum, although additional fabrication processes, like electron beam lithography, are needed, making the whole process more complicated.

The easiest way to create a metamaterial is to consider planar multilayer nanostructures composed from multiple metal-dielectric layers [7,8]. Then creating a uniaxial dielectric permittivity that has the in-plane components be equal and different from the perpendicular one, $\varepsilon_x = \varepsilon_y \neq \varepsilon_z$. The uniaxial material has a hyperbolic dispersion relation and support polariton modes [9–11]. These modes can be excited by a QE placed in their vicinity leading to a significant reduction of its lifetime, which preferentially relaxes by exciting the hyperbolic modes [12–15]. These types of structures have their main response in the visible part of the spectrum, due to the use of noble metals.

A natural hyperbolic material that has attracted a lot of attention in the last few years is hexagonal boron nitride (*h*-BN), which has an optical response in the terahertz regime and supports phonon polariton (PhP) modes [16,17]. The PhP modes have a large momentum mismatch with the applied plane wave excitation; thus, when the EM field is scattered from a metallic tip or a scatterer provides the necessary high-k wave vector components needed to be experimentally probed [18–20]. When a QE is considered interacting with a *h*-BN or a *h*-BN/graphene layer, the high-k wave vector components are provided directly by its near field [21–23].

The interaction strength between a QE and its environment is estimated through the Purcell factor. The Purcell factor shows how much the relaxation rate of the QE is enhanced or inhibited compared to its free space value; in the weak-coupling regime, the light-matter interactions are connected with the incoherent light emission. When the Purcell factor of the QE is enhanced several orders of magnitude, then the above picture ceases to be valid and the light-matter interaction needs to be described in the strong-coupling regime [4,24]. At the strong-coupling regime, the QE exchange energy coherently with its environment. Enhancing the relaxation rate is important for various applications such as single photon emission devices [25]. Although special care must be taken in order to be certain if the system under consideration operates in the strong-coupling regime, where the signal from the emission spectrum of the active material is important [26,27].

The interaction between a QE placed in a nanostructured environment has been extensively investigated experimentally and theoretically considering different material environment both in the weak and strong coupling regimes. Considering noble metal nanostructures [7,28–34], graphene [35–39], and transition metal dichalcogenides [40–47]. In this paper we consider the interaction of a QE with an *h*-BN layer in

*KARANIKOLAS.Vasileios@nims.go.jp

the strong-coupling regime, by investigating the emission spectrum of the combined system. The strong-coupling regime is theoretically investigated considering the *h*-BN material platform.

We start by giving the QE/*h*-BN layer interaction in the context of non-Hermitian description of the light matter interactions. We analyze the PhP modes supported by the *h*-BN layer; the penetration depth defines the length scale within which a QE can be placed and have the most efficient interaction with the *h*-BN layer. In the results part we investigate the emission properties of the QE in the weak and strong coupling regimes. We investigate the emission spectrum of the QE and we analyze its dependence on the free-space relaxation rate and the position of the QE.

II. MATHEMATICAL FORMULATION AND MATERIAL PARAMETERS

A. Emission spectrum calculation in the weak and strong-coupling regime

The quantum emitters (QEs) considered in this paper are approximated as two-level systems. Various emitters, such as atoms, molecules, quantum wells, and dots can be approached as two-level systems. The ground state of the QE is denoted as $|g\rangle$, and the excited state as $|e\rangle$. The transition frequencies from the excited to the ground state and the transition dipole matrix element are denoted as ω_0 and $\boldsymbol{\mu}$, respectively. An excited quantum emitter interacts with its environment through the electromagnetic field and relaxes from its excited state to the ground state by emitting a photon or exciting any of the dressed states supported by its environment. As we will see in the following section the *h*-BN layer supports phonon polariton (PhP) modes, which are the main path of relaxation for the QE. The initial state of the system is denoted as $|i\rangle = |e\rangle \otimes |0\rangle$, where the QE is in the excited state and the electromagnetic field is in its vacuum state. The QE will relax to the medium dressed states and therefore the EM field will be in a $|1(\mathbf{k}, p)\rangle = \hat{f}_i^{\dagger}(\mathbf{r}, \omega)|0\rangle$ state; p and $\mathbf{k}$ are the polarization and wave vector, respectively. The final state of the entire system therefore has the form $|f\rangle = |g\rangle \otimes \hat{f}_i^{\dagger}(\mathbf{r}, \omega)|0\rangle$. By applying Fermi's golden rule and summing over all final states, the expression for the relaxation rate Γ is given by $\Gamma(\mathbf{r}, \omega) = \frac{2\omega^2\mu^2}{\hbar\varepsilon_0 c^2}\hat{\mathbf{n}} \cdot \mathrm{Im}\,\mathfrak{G}(\mathbf{r}, \mathbf{r}, \omega) \cdot \hat{\mathbf{n}}$, where $\hat{\mathbf{n}}$ is a unit vector along the direction of the transition dipole moment $\boldsymbol{\mu}$, and $\mathfrak{G}(\mathbf{r}, \mathbf{s}, \omega)$ is the Green's tensor representing the response of the geometry under consideration to a pointlike excitation [48–51].

In order to quantify the influence of the environment on the QE emission, the Purcell factor of the QE is introduced as:

$$\tilde{\Gamma} = \frac{\Gamma}{\Gamma_0} = \sqrt{\varepsilon} + \frac{6\pi c}{\omega}\hat{n}_i \mathrm{Im}\,\mathfrak{G}_{\mathrm{S}}^{ii}(\mathbf{r}, \mathbf{r}, \omega)\hat{n}_i, \tag{1}$$

where $i = x, z$ defines the different transition dipole moment orientations, ε is the permittivity of the host medium, Γ_0 is the free-space relaxation rate, $\Gamma_0 = \omega^3\mu^2/3\pi c^3\hbar\varepsilon_0$, and $\mathfrak{G}_{\mathrm{S}}$ is the scattering part of the Green's tensor calculated at the QE's position $\mathbf{r}$.

Equation (1) is valid for the case the QE/*h*-BN layer interaction is in the weak-coupling regime where the light emission is incoherent and the QE follows an exponential relaxation path. For the strong-coupling regime a different approach is needed to describe the QE/*h*-BN layer interaction, where the strength of energy exchange between the QE/nanostructure combined system is given through the spectral density from the expression

$$J(\omega_0, \omega, \mathbf{r}) = \frac{\Gamma_0(\omega_0)}{2\pi}\tilde{\Gamma}_z(\omega, \mathbf{r})\left(\frac{\omega}{\omega_0}\right)^3, \tag{2}$$

where ω_0 is the energy difference between the ground and the excited states of the QE, $\Gamma_0(\omega_0)$ is the relaxation rate of the QE in free space, and $\tilde{\Gamma}_z$ is the normalized SE rate, given by Eq. (1). We observe that the higher the enhancement factor the stronger the coupling of the QE with its environment. Also, the value of the transition dipole moment is very important for approaching the strong-coupling limit; the higher its value the smaller value of the Purcell factor is needed [24]. In the results part we connect the transition dipole moment of the QE with its free-space lifetime. The light emitted spectrum of the QE is given by $S(\omega, \mathbf{r}) = \frac{1}{2\pi}\int_0^{\infty} dt_2 \int_0^{\infty} dt_1 e^{-i\omega(t_2-t_1)}\langle\hat{\mathbf{E}}^{(-)}(t_2, \mathbf{r}) \cdot \hat{\mathbf{E}}^{(+)}(t_1, \mathbf{r})\rangle$ where, after carrying out the calculations, the full expression has the form

$$S(\omega, \mathbf{r}) = \frac{1}{2\pi}\left|\frac{\frac{\mu^2\omega^2}{\varepsilon_0 c^2}\hat{\mathbf{n}} \cdot \mathfrak{G}(\omega, \mathbf{r}, \mathbf{r}_d)}{\omega_1 - \omega - \int_0^{\infty} d\omega' J(\omega_0, \omega', \mathbf{r})\frac{1}{\omega'-\omega}}\right|^2, \tag{3}$$

$\mathbf{r}_d$ is the position of the signal detection and $\mathbf{r}$ is the position placed on the QE, and ω is the emission frequency of the combined QE/*h*-BN system [34,52–54].

B. *h*-BN material parameters and dispersion relation

The optical response of the *h*-BN material is given by its dielectric permittivity

$$\varepsilon_i(\omega) = \varepsilon_{\infty,i}\left(1 + \frac{(\omega_{\mathrm{LO},i})^2 - (\omega_{\mathrm{TO},i})^2}{(\omega_{\mathrm{LO},i})^2 - \omega^2 - i\omega\gamma_i}\right), \tag{4}$$

where for $i = z$ is the out of plane dielectric permittivity, with the parameters: $\varepsilon_{\infty,z} = 4.87$, $\omega_{\mathrm{TO},z} = 0.096$ eV, $\hbar\omega_{\mathrm{LO},z} = 0.103$ eV, and $\gamma_z = 0.62$ *m*eV; for $i = x$ is the in-plane dielectric permittivity, with the parameters: $\varepsilon_{\infty,x} = 2.95$, $\omega_{\mathrm{TO},x} = 0.170$ eV, $\omega_{\mathrm{LO},x} = 0.200$ eV, and $\gamma_x = 0.50$ *m*eV. *h*-BN is a natural uniaxial material, the two dielectric permittivities over the two spatial dimensions lead to the existence of two Reststrahlen bands, (a) the lower band, when $\mathrm{real}(\varepsilon_z) < 0$ and $\mathrm{real}(\varepsilon_x) > 0$ corresponding to Type I hyperbolicity and (b) the upper band, when $\mathrm{real}(\varepsilon_z) > 0$ and $\mathrm{real}(\varepsilon_x) < 0$ corresponding to Type II hyperbolicity [16,21,55,56]. The Reststrahlen bands are the spectral intervals between the longitudinal (LO) and transverse (TO) optical phonon frequencies. In Fig. 1(a) we present the two Reststrahlen bands and we also point out the areas where the Type I and II hyperbolicities exist.

When a *h*-BN layer is considered, then two dielectric/*h*-BN interfaces are involved. Throughout this paper we consider the dielectric permittivity of the host medium to be the free space, $\varepsilon_1 = \varepsilon_3 = 1$. In Figs. 1(b)–1(e) the dispersion relation $\hbar\omega(k_\rho)$ for the *h*-BN layer, the relation between the applied energy and the in-plane wave vector, is presented.

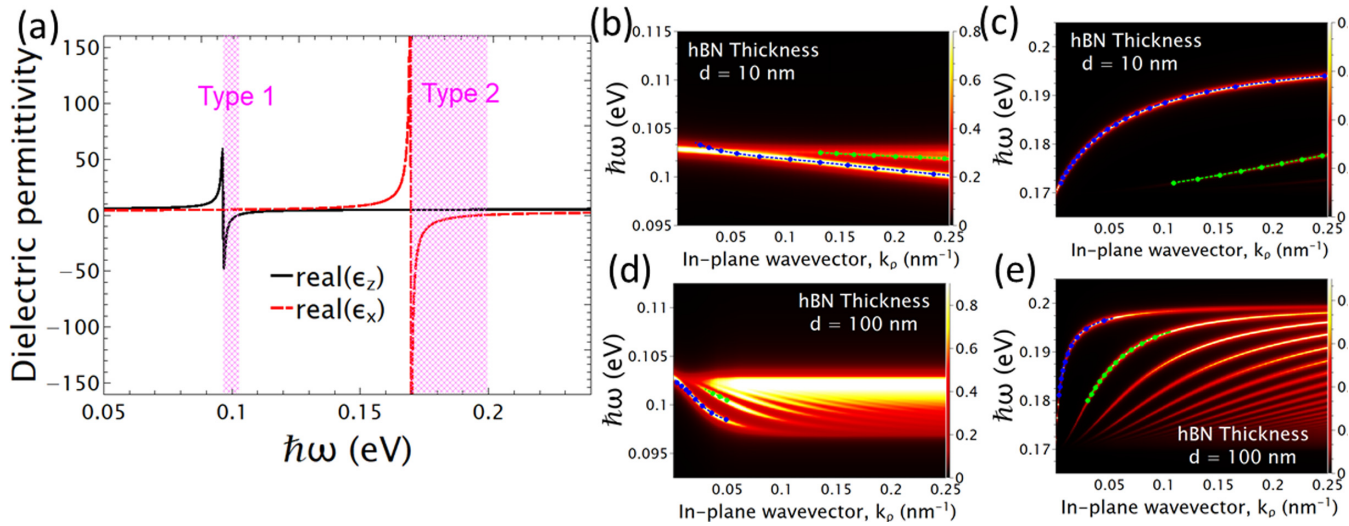

FIG. 1. (a) Real part of the dielectric permittivity of the in plane, $\varepsilon_x(\omega)$, and out of plane, $\varepsilon_z(\omega)$, dielectric permittivities of h-BN layer. (b)–(e) Dispersion relation curve $\hbar\omega(k_\rho)$; we plot the energy loss function connected with the layer reflection coefficient. Two thicknesses are considered, $d = 10$ and 100 nm, at panels (b),(c) and (d),(e), respectively. We focus on the two Reststrahlen bands, the lower, (b),(d), and higher, (c),(e). The blue dashed-dotted line gives the first phonon polariton mode for each band and the green dashed-dotted line gives the second mode.

To do so in Figs. 1(b)–1(e) we plot the imaginary part of the integrant of the scattering part of the Green's tensor $d\mathfrak{G}_S^{ij}(\mathbf{r}, \mathbf{r}, \omega)$, which includes the poles of the reflection coefficient due to the PhP of the h-BN layer. The quantity plotted at Figs. 1(b)–1(e) is connected with the energy loss spectroscopy quantity, where the bright colors show the PhP modes.

We consider two thicknesses of the h-BN layer, $d = 10$ nm at Figs. 1(b) and 1(c) and $d = 100$ nm at Figs. 1(d) and 1(e), for the Type I, Figs. 1(b) and 1(d), and Type II, Figs. 1(c) and 1(e), hyperbolicities [16,56]. We observe that as the thickness of the h-BN layer is increased the number of polariton modes also is increased, due to multiple reflections supported in the h-BN layer. In all panels of Figs. 1(b)–1(e) the free space light line is not visible and lies very close to the y axis of the plots; this is an indication that the PhP modes cannot be excited by direct light illumination due to the momentum mismatch. The first order PhP mode in each panel is given by the blue dashed-dotted line and the second order hyperbolic mode is given by the green dashed-dotted line. We observe that the PhP modes of the thinner h-BN layers are more dispersive, since they are excited for higher in-plane wave vector k_ρ values, thus these modes are tightly confinement to the h-BN layer.

The PhP modes are characterized by their confinement over the perpendicular dimension at the dielectric/h-BN interface, the degree of confinement over the dielectric media is given by the penetration depth δ, which is defined as $\delta = 1/(2\mathrm{Im}(k_{z1}))$, where $k_{z1} = \sqrt{k_1^2 - k_\rho^2}$; due to the fact that the h-BN material supports PhP modes that are highly dispersive $k_{z1} \approx ik_\rho$ and then $\delta = 1/(2k_\rho)$ [5]. In Fig. 2 we present the penetration depth δ of the first and second hyperbolic modes presented in Figs. 1(b)–1(e) for the lower and higher energy Reststrahlen bands; the h-BN layer thickness is $d = 10$ and 100 nm. For both panels of Fig. 2 we observe that the confinement of light in the perpendicular dimension is at least two orders of magnitude smaller than the free space wavelength λ, $\delta/\lambda < 10^{-2}$. For both Reststrahlen bands we observe that the higher order modes are more tightly confined to the h-BN layer than the lower order. Moreover, the PhP penetration depth is larger for the higher energy Reststrahlen band compared to the lower one. The penetration depth increases as the energy is increased for the lower energy Reststrahlen band, while the opposite behavior is observed for the higher Reststrahlen band. Thus, the relaxation rate of the QE depends strongly on the transition energy of the QE, if it is placed at a fixed position above the h-BN layer. The penetration depth is an important feature of the PhP modes that can be exploited for possible biosensor applications.

When a thin noble metal film is considered, the penetration depth of the supported plasmon polariton mode is reduced for increasing the applied energy [57]. The opposite behavior is observed for the lower energy Reststrahlen band for a h-BN layer, thus the coupling of a nearby placed QE will depend on its transition energy if it is within the lower or higher energy Reststrahlen bands.

III. RESULTS PART

A. Purcell factor

The relaxation process of a QE is described by the interaction with its environment through the electromagnetic field. The Purcell factor allows us to understand the interaction strength between a QE and the h-BN layer. We focus on a QE with a z-transition dipole moment, because its coupling with a planar nanostructure is higher than the case we have of an x-transition dipole moment. In Figs. 3(a) and 3(b) we present the Purcell factor of a QE placed 100 nm above a h-BN layer of thickness d, varying its emission energy, $\hbar\omega_0$. The position of the QE is $\mathbf{r} = (0, 0, d + 100\ \mathrm{nm})$ in Cartesian coordinates. We consider the two Reststrahlen bands, the lower in Fig. 3(a) and higher in Fig. 3(b). We observe that when the emission of the QE excites the PhP mode supported by the h-BN layer then

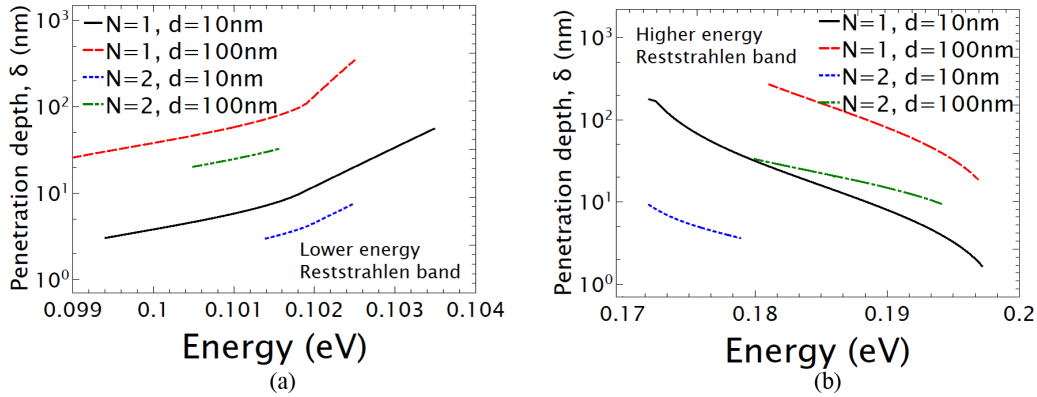

FIG. 2. Penetration depth δ of the PhP mode of the h-BN layer is presented. The first and second polariton modes are shown for the lower (a) and higher (b) Reststrahlen bands.

the Purcell factor is enhanced above two orders of magnitude, compared to the free space value.

At the lower energy band, Fig. 3(a), we observe that as the h-BN thickness is increased the value of the Purcell factor of the QE is also increased but the peak value of the Purcell factor is only slightly redshifted; this effect can be understood by observing that the PhP modes for the 10 nm and 100 nm h-BN layer thickness are close, Figs. 1(b) and 1(d). For the higher energy Reststrahlen band, we observe that the Purcell factor peak is blueshifted as the thickness of the h-BN is increased. The blueshift is explained by the plot of the penetration depth from Fig. 2(b), where for the 10 nm thickness the $\delta = 100$ nm is at energy of $\hbar\omega_0 = 0.174$ eV, which matches the peak energy observed at Fig. 3(b), and for the thickness of $d = 100$ nm the $\delta = 100$ nm is at $\hbar\omega_0 = 0.188$ eV. The above shows that there is a nontrivial distance dependence of the QE/h-BN layer interaction; as the QE/h-BN separation or h-BN layer thickness are varied, the penetration depth provides the information needed.

The distance dependence of the Purcell factor of a QE above a h-BN layer is analyzed in Figs. 3(c) and 3(d). We consider different values for the layer thickness,

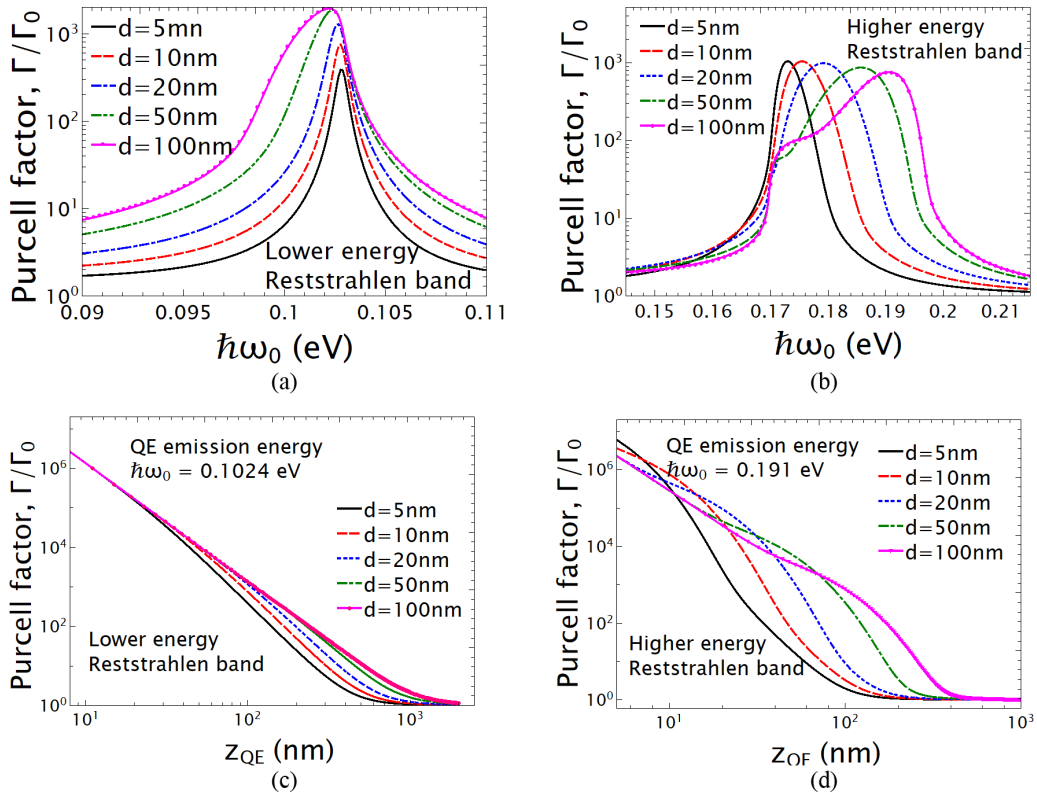

FIG. 3. Purcell factor of a quantum emitter with a z transition dipole moment, interacting with the h-BN layer of thickness d. (a),(b) The QE is placed at $\mathbf{r} = (0, 0, d + 100\ \text{nm})$ and we vary its emission energy. (c),(d) The position of the QE is varied for transition energies of (c) $\hbar\omega_0 = 0.1024$ eV and (d) $\hbar\omega_0 = 0.191$ eV. The h-BN layer thicknesses considered are $d = 5$, 10, 20, 50, and 100 nm. We consider the (a),(c) lower and (b),(d) higher energy Reststrahlen bands.

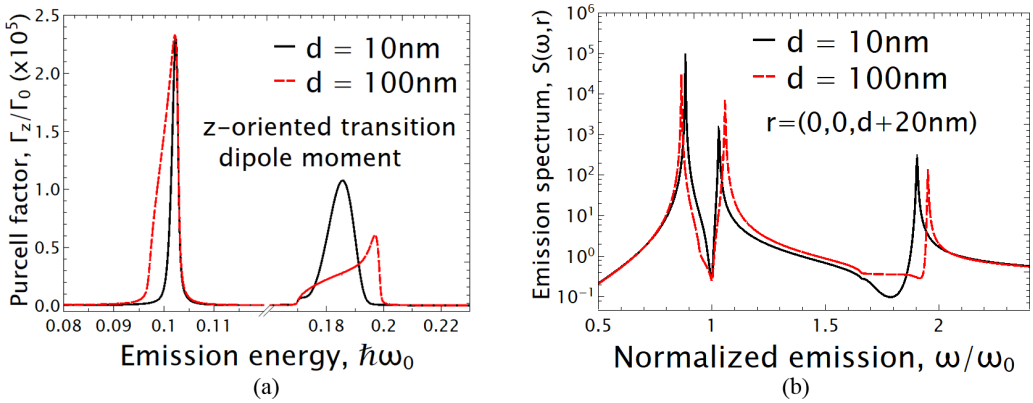

FIG. 4. We consider a quantum emitter, placed at $\mathbf{r}_{\rm QE} = (0, 0, d + 20\ {\rm nm})$, above the h-BN layer; two layer thicknesses are considered $d = 10$ nm and 100 nm. (a) Purcell factor of the QE. (b) Emission spectrum of the QE, with a transition energy of $\hbar\omega_0 = 0.1024$ eV, the emission energy is normalized to ω_0. The transition dipole moment of the QE is along z and the free-space relaxation rate is $\tau = 1$ ns.

$d = 5$, 10, 20, 50, and 100 nm. Two different values of the transition energy of the QE are considered; $\hbar\omega_0 = 0.1024$ eV, Fig. 3(c), and $\hbar\omega_0 = 0.191$ eV, Fig. 3(d). In Fig. 3(c) the emission energy of the QE, $\hbar\omega_0 = 0.1024$ eV, matching the energy at which is observed the peak value of the Purcell of the QE interacting with a h-BN layer of thickness of $d = 5$ nm, when it is positioned at 100 nm above the layer, see Fig. 3(a). We observe that the distance dependence does not vary substantially for the different values of the layer thickness d. As the QE/h-BN layer separation is increased the Purcell factor follows a power law dependence, which implies an excitation of bulk modes.

A more interesting behavior is observed when the transition energy of the QE is in the higher energy Reststrahlen band. From Fig. 3(b) we observe that the peak position of the Purcell factor spectrum of the QE, over the spectral range, changes as the h-BN layer thickness changes. In Fig. 3(d) the emission energy of the QE matches the peak value of the Purcell factor for a layer thickness of $d = 100$ nm. We observe that for the different thicknesses of the h-BN layer and for separation distances smaller than 15 nm, the Purcell factor has a power law dependence similar to Fig. 3(c), a sign that the QE relaxes by exciting bulk modes. As the QE/h-BN layer separation is increased, we observe that for the layer thickness of $d = 100$ nm the Purcell factor follows an exponential distance dependence, a sign that the PhP modes are the main path of relaxation for the QE. Further increasing the QE/h-BN layer separation, the Purcell factor of the QE reverts to its free-space value, where for $d = 100$ nm the Purcell factor has values above $\Gamma/\Gamma_0 > 100$ for separation distance above 200 nm. For the thinner h-BN layers the Purcell factor reverts to the free-space value for smaller separations. The above analysis shows the importance of using the h-BN layer as a platform for sensor applications at the THz regime.

B. Spontaneous emission spectrum

In Figs. 3(a) and 3(b) we focus on separation distances between the QE and the h-BN layer of 100 nm; at these distances the relaxation rate of the QE is described at the weak-coupling regime, meaning that QE relaxes from the exited to the ground state by following an exponential decay which is given by $\exp\left(-\Gamma_0\tilde{\Gamma}(\mathbf{r}, \omega_0)t\right)$. In Figs. 3(c) and 3(d) we observe that as the separation between the QE and the h-BN layer is decreased, the Purcell factor of the QE value is higher than 10^5 for separation distances below 20 nm. At these separation distances the emission spectrum of the QE needs to be described in the strong-coupling regime using Eq. (3). The QEs considered have a transition energy at the far-infrared part of the spectrum, quantum wells, through intersubband transitions, and molecules, through vibrational excitations, have optical response in the same part of the electromagnetic spectrum [58–61].

In Fig. 4(a) we present the Purcell factor of a QE that is placed 20 nm above an h-BN layer, considering two layer thicknesses. We observe that the Purcell factor reaches values above 10^5 at energies that the PhP modes are excited. For more details check Figs. 3(c) and 3(d) and the relevant discussion. In Fig. 4(b) we consider a QE with transition energy of $\hbar\omega_0 = 0.1024$ eV at the lower energy band, Eq. (4); we observe from Fig. 4(a) that there is an enhancement of the relaxation rate of the QE of 2.29×10^5 times, compared to the free space value, and also with a FWHM of $\hbar\Delta\omega = 0.0015$ eV, for a layer thickness of $d = 10$ nm, and an enhancement of 2.32×10^5 and $\hbar\Delta\omega = 0.0037$ eV, for the layer thickness of $d = 100$ nm. The aforementioned quantities give a quality factor, $\omega_0/\Delta\omega$, value of 68 and 28 for the $d = 10$ and 100 nm, respectively. The Purcell enhancement and quality factors values are a clear indication that the system under consideration does not operate in the weak-coupling regime.

In Fig. 4(b) we present the emission spectrum of the combined QE/h-BN layer system. The emission energy, x axis, is normalized to the transition energy $\hbar\omega_0 = 0.1024$ eV of the QE. The free-space relaxation rate is $\tau = 1$ ns. We observe that the emission spectrum presents two peaks which they are away from the transition energy of the QE. Thus, we observe an energy splitting of $\Omega/\omega_0 = 15\%$ and $\Omega/\omega_0 = 20\%$ between them, for the thicknesses of $d = 10$ and 100 nm, respectively. The Rabi splitting $\hbar\Omega$ is connected with the coherent exchange of energy between the elements of the total system, here the QE and the h-BN layer.

From Eq. (3) and Fig. 4 it is obvious that in order for the system under consideration to operate in the strong coupling regime we need to have a large Purcell factor value of the

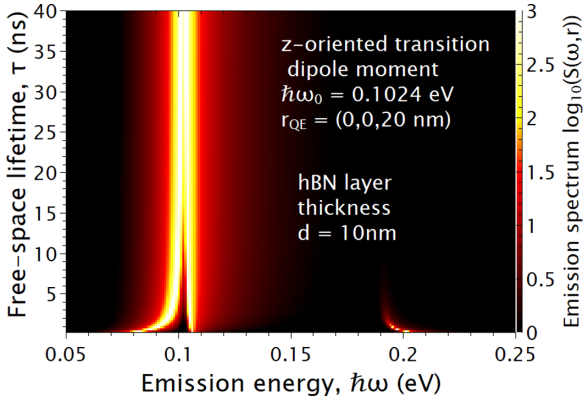

FIG. 5. (a) Contour plot of the emission spectrum, $S(\omega, \mathbf{r})$, of a QE interacting with the h-BN layer for varying the emission energy and the free space lifetime τ. The transition energy of the QE is $\hbar\omega_0 = 0.1024$ eV and its dipole moment is along z. The h-BN layer has a thickness of $d = 10$ nm.

QE at the transition energy, $\hbar\omega_0$, and depends on the free-space relaxation rate τ. In Fig. 5 we present the logarithm of the emission spectrum $S(\omega, \mathbf{r})$ of a QE when it interacts with the h-BN layer, where we vary the emission energy, $\hbar\omega$, and the free-space lifetime of the QE, τ. The transition energy of the QE is $\hbar\omega_0 = 0.1024$ eV and its position is 20 nm above the h-BN layer, with a thickness of $d = 10$ nm. We observe that for small values of the free-space lifetime, $\tau < 4$ ns, a pronounced splitting in the emission spectrum. Also, for $\tau < 4$ ns there is one more emission peak at the upper Reststrahlen band; this third peak is connected with the higher energy peak of Purcell factor observed in Fig. 4(a). As the value of the free-space relaxation rate is increased the Rabi splitting is reduced and for values of $\tau > 15$ ns the total system QE/h-BN layer reverts to the weak-coupling regime. For the free-space lifetime of $\tau = 0.5$ ns the Rabi splitting between the first two peaks has a value of $\hbar\Omega = 0.0236$ eV, $\Omega/\hbar_0 = 23.5\%$, and the splitting between the first and the third peak is $\hbar\Omega = 0.1191$ eV, $\Omega/\omega_0 = 116.3\%$. For $\tau > 15$ ns the emission spectrum presents a single peak, thus the QE/h-BN layer operates in the weak-coupling regime.

The free-space lifetime τ of the QE is connected to the value of its transition dipole moment μ through the relation $1/\tau = \omega_0^3\mu^2/3\pi c^3\hbar\varepsilon_0$. For a QE with transition energy $\hbar\omega_0 = 0.1024$ eV and $\tau = 1$ ns the transition dipole moment has a value $\mu = 2.4 \times 10^3$ D and for $\tau = 40$ ns the dipole moment has a value $\mu = 3.8 \times 10^2$ D. For comparison, in Ref. [61] the vibrational state lifetime of the investigated molecules is $\tau = 0.01$ ns at transition energy of $\hbar\omega_0 = 0.20$ eV, then the transition dipole moment has a value $\mu = 8.2 \times 10^6$ D. Thus, the values considered are within existing physical systems.

In Fig. 6 we present a contour plot of the logarithm of the spontaneous emission spectrum, $\log(S(\mathbf{r}, \omega))$, of a QE placed above the h-BN layer, of $d = 10$ nm thickness, while we vary its position. The QE is placed at $\mathbf{r}_{\rm QE} = (0, 0, z_{\rm QE})$ above the h-BN layer. Two transition energies of the QE are considered (a) $\hbar\omega_0 = 0.1024$ eV and (b) $\hbar\omega_0 = 0.1755$ eV; these energies are the peak values of the Purcell factor of the QE when it interacts with a 10 nm h-BN layer, Fig. 3(a). The transition dipole moment of the QE is along z and its free-space relaxation rate is $\tau = 1$ ns. When the transition energy of the QE, $\hbar\omega_0 = 0.1024$ nm, is in the lower Reststrahlen energy band, Fig. 6(a), we observe that there is a Rabi splitting in the emission spectrum of the QE. The Rabi splitting is maintained for QE/h-BN layer separations of 30 nm. Further increasing the separation between the QE/h-BN layer, the system reverts to the weak-coupling regime where a single emission peak is observed. When the transition energy of the QE, $\hbar\omega_0 = 0.1756$ eV, in the upper Reststrahlen energy band, Fig. 6(a), we also observe a Rabi splitting on the transition energy of the QE. The Rabi splitting is present for separations distances between the QE and the h-BN layer up to 50 nm.

When we compare the two contour plots for the two transition energies, first we observe that for the transition energy of the QE in the lower energy band, $\hbar\omega_0 = 0.1024$ eV, there are three peeks in the emission spectrum for $z_{\rm QE} < 25$ nm, while for $\hbar\omega_0 = 0.1756$ eV there are two. This effect is connected with the fact that the Purcell factor spectrum of the QE in the lower energy PhP band resonance is much sharper than the upper one, thus has a smaller contribution to the emission spectrum. Secondly, we observe that for the transition energy of $\hbar\omega_0 = 0.1756$ eV the Rabi splitting exists for larger distances, compared to the transition energy of $\hbar\omega_0 = 0.1024$ eV; this is due to the fact that for emission energies in the higher Reststrahlen energy band the penetration depth δ is larger than the case of emission energies at the

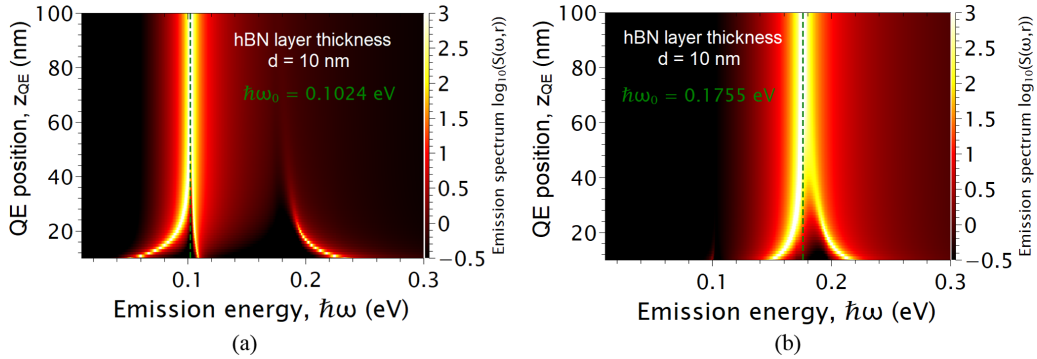

FIG. 6. Contour plot of the logarithm of the spontaneous emission spectrum, $\log(S(\mathbf{r}, \omega))$, of a QE placed above the h-BN layer, of $d = 10$ nm thickness, while we vary its position. The QE is placed at $\mathbf{r}_{\rm QE} = (0, 0, z_{\rm QE})$ above the h-BN layer. Two transition energies of the QE are considered (a) $\hbar\omega_0 = 0.1024$ eV and (b) $\hbar\omega_0 = 0.1755$ eV. The transition dipole moment of the QE is along z and the free-space relaxation rate is $\tau = 1$ ns.

lower, thus the QE can excite more efficiently the PhP modes, Fig. 2, further highlighting the difference between the Type I and II hyperbolicities supported by the h-BN layer. Since the h-BN layer is a natural hyperbolic material there is no need for additional fabrication steps; both hyperbolicity types are supported by the same layer at different energy bands.

IV. CONCLUSION AND FUTURE STEPS

In this paper we investigate the emission spectrum of a QE interacting with a h-BN layer in the weak and strong-coupling regimes. We start by describing the material parameters of the h-BN material. The h-BN layer supports phonon polaritons (PhP) modes that can lead to a 10^4 confinement of the light for the lower and higher energy Reststrahlen bands.

When a QE is placed in proximity to the h-BN layer, within the penetration depth of the phonon mode, the Purcell factor is enhanced several orders of magnitude, above 2 for a separation of 100 nm. The main path of relaxation of the QE is the phonon polariton modes.

At smaller QE/h-BN separation distances, high values of the Purcell factor of the QE are exhibited, then the light-matter interactions are described in the strong-coupling regime. The realization of the strong-coupling regime can be experimentally detected in the emission spectrum of the QE, through the Rabi splitting at its transition energy. Moreover, in the emission spectrum three peaks are observed due to the interaction between the emission energy of the QE and the two peaks in the Purcell factor observed in the lower and higher Reststrahlen bands.

Our analysis clearly demonstrates the differences in the emission spectrum of the weak and strong-coupling regimes. The form of the emission spectrum of the QE, interacting with a h-BN layer, depends on its position, transition energy, and free space relaxation rate.

[1] E. N. Economou, Phys. Rev. **182**, 539 (1969).
[2] W. L. Barnes, J. Modern Opt. **45**, 661 (1998).
[3] P. Vasa, R. Pomraenke, S. Schwieger, Y. I. Mazur, V. Kunets, P. Srinivasan, E. Johnson, J. E. Kihm, D. S. Kim, E. Runge, G. Salamo, and C. Lienau, Phys. Rev. Lett. **101**, 116801 (2008).
[4] P. Vasa and C. Lienau, ACS Photonics **5**, 2 (2018).
[5] W. L. Barnes, J. Opt. A **8**, S87 (2006).
[6] J. B. Khurgin, Nat. Nanotechnol. **10**, 2 (2015).
[7] H. N. S. Krishnamoorthy, Z. Jacob, E. Narimanov, I. Kretzschmar, and V. M. Menon, Science **336**, 205 (2012).
[8] A. Poddubny, I. Iorsh, P. Belov, and Y. Kivshar, Nat. Photon. **7**, 948 (2013).
[9] Z. Huang and E. E. Narimanov, Opt. Express **21**, 15020 (2013).
[10] V. E. Babicheva, M. Y. Shalaginov, S. Ishii, A. Boltasseva, and A. V. Kildishev, Opt. Express **23**, 31109 (2015).
[11] V. E. Babicheva, J. Opt. **19**, 124013 (2017).
[12] A. N. Poddubny, P. A. Belov, and Y. S. Kivshar, Phys. Rev. A **84**, 023807 (2011).
[13] Z. Jacob, I. I. Smolyaninov, and E. E. Narimanov, Appl. Phys. Lett. **100**, 181105 (2012).
[14] W. D. Newman, C. L. Cortes, and Z. Jacob, J. Opt. Soc. Am. B **30**, 766 (2013).
[15] Y. Moritake, K. Nakayama, T. Suzuki, H. Kurosawa, T. Kodama, S. Tomita, H. Yanagi, and T. Ishihara, Phys. Rev. B **90**, 075146 (2014).
[16] J. D. Caldwell, A. V. Kretinin, Y. Chen, V. Giannini, M. M. Fogler, Y. Francescato, C. T. Ellis, J. G. Tischler, C. R. Woods, A. J. Giles, M. Hong, K. Watanabe, T. Taniguchi, S. A. Maier, and K. S. Novoselov, Nat. Commun. **5**, 5221 (2014).
[17] J. D. Caldwell, I. Aharonovich, G. Cassabois, J. H. Edgar, B. Gil, and D. N. Basov, Nat. Rev. Mater. **4**, 552 (2019).
[18] J. Duan, R. Chen, J. Li, K. Jin, Z. Sun, and J. Chen, Adv. Mater. **29**, 1702494 (2017).
[19] A. Fali, S. T. White, T. G. Folland, M. He, N. A. Aghamiri, S. Liu, J. H. Edgar, J. D. Caldwell, R. F. Haglund, and Y. Abate, Nano Lett. **19**, 7725 (2019).
[20] P. Pons-Valencia, F. J. Alfaro-Mozaz, M. M. Wiecha, V. Biolek, I. Dolado, S. Vélez, P. Li, P. Alonso-González, F. Casanova, L. E. Hueso, L. Martín-Moreno, R. Hillenbrand, and A. Y. Nikitin, Nat. Commun. **10**, 3242 (2019).
[21] A. Kumar, T. Low, K. H. Fung, P. Avouris, and N. X. Fang, Nano Lett. **15**, 3172 (2015).
[22] Y. Jiang, X. Lin, T. Low, B. Zhang, and H. Chen, Laser Photon. Rev. **12**, 1800049 (2018).
[23] N. A. Kostina, D. A. Kislov, A. N. Ivinskaya, A. Proskurin, D. N. Redka, A. Novitsky, P. Ginzburg, and A. S. Shalin, ACS Photon. **7**, 425 (2020).
[24] D. G. Baranov, M. Wersall, J. Cuadra, T. J. Antosiewicz, and T. Shegai, ACS Photon. **5**, 24 (2018).
[25] I. Aharonovich, D. Englund, and M. Toth, Nat. Photon. **10**, 631 (2016).
[26] C. Tserkezis, A. I. Fernández-Domínguez, P. A. D. Gonçalves, F. Todisco, J. D. Cox, K. Busch, N. Stenger, S. I. Bozhevolnyi, N. A. Mortensen, and C. Wolff, Rep. Prog. Phys. **83**, 082401 (2020).
[27] M. Pelton, S. D. Storm, and H. Leng, Nanoscale **11**, 14540 (2019).
[28] M. S. Tame, K. R. McEnery, S. K. Ozdemir, J. Lee, S. A. Maier, and M. S. Kim, Nat. Phys. **9**, 329 (2013).
[29] D. Lu, J. J. Kan, E. E. Fullerton, and Z. Liu, Nat. Nanotechnol. **9**, 48 (2014).
[30] T. B. Hoang, G. M. Akselrod, C. Argyropoulos, J. Huang, D. R. Smith, and M. H. Mikkelsen, Nat. Commun. **6**, 7788 (2015).
[31] P. Torma and W. L. Barnes, Rep. Progr. Phys. **78**, 013901 (2015).
[32] R. Chikkaraddy, B. de Nijs, F. Benz, S. J. Barrow, O. A. Scherman, E. Rosta, A. Demetriadou, P. Fox, O. Hess, and J. J. Baumberg, Nature (London) **535**, 127 (2016).
[33] I. Thanopulos, V. Yannopapas, and E. Paspalakis, Phys. Rev. B **95**, 075412 (2017).
[34] N. Iliopoulos, I. Thanopulos, V. Yannopapas, and E. Paspalakis, Phys. Rev. B **97**, 115402 (2018).
[35] F. H. L. Koppens, D. E. Chang, and F. J. Garcia de Abajo, Nano Lett. **11**, 3370 (2011).
[36] L. Gaudreau, K. J. Tielrooij, G. E. D. K. Prawiroatmodjo, J. Osmond, F. J. G. de Abajo, and F. H. L. Koppens, Nano Lett. **13**, 2030 (2013).

[37] K. J. Tielrooij, L. Orona, A. Ferrier, M. Badioli, G. Navickaite, S. Coop, S. Nanot, B. Kalinic, T. Cesca, L. Gaudreau, Q. Ma, A. Centeno, A. Pesquera, A. Zurutuza, H. de Riedmatten, P. Goldner, F. J. Garcia de Abajo, P. Jarillo-Herrero, and F. H. L. Koppens, Nat. Phys. **11**, 281 (2015).
[38] F. J. Garcia de Abajo, ACS Photonics **1**, 135 (2014).
[39] V. D. Karanikolas, C. A. Marocico, and A. L. Bradley, Phys. Rev. B **93**, 035426 (2016).
[40] L. Britnell, R. M. Ribeiro, A. Eckmann, R. Jalil, B. D. Belle, A. Mishchenko, Y.-J. Kim, R. V. Gorbachev, T. Georgiou, S. V. Morozov, A. N. Grigorenko, A. K. Geim, C. Casiraghi, A. H. C. Neto, and K. S. Novoselov, Science **340**, 1311 (2013).
[41] Y. N. Gartstein, X. Li, and C. Zhang, Phys. Rev. B **92**, 075445 (2015).
[42] D. Prasai, A. R. Klots, A. K. M. Newaz, J. S. Niezgoda, N. J. Or, C. A. Escobar, A. Wynn, E. Anatoly, G. K. Jennings, S. J. Rosenthal, and K. I. Bolotin, Nano Lett. **15**, 4374 (2015).
[43] A. Raja, A. M. Castillo, J. Zultak, X.-X. Zhang, Z. Ye, C. Roquelet, D. A. Chenet, A. M. V. D. Zande, P. Huang, J. C. Hone, D. R. Reichman, L. E. Brus, T. F. Heinz, A. Raja, A. M. Castillo, and J. Zultak, Nano Lett. **16**, 2328 (2016).
[44] H. Zang, P. K. Routh, Y. Huang, J.-S. Chen, E. Sutter, P. Sutter, and M. Cotlet, ACS Nano **10**, 4790 (2016).
[45] V. Karanikolas, I. Thanopulos, and E. Paspalakis, Opt. Lett. **44**, 2049 (2019).
[46] I. Thanopulos, V. Karanikolas, and E. Paspalakis, Opt. Lett. **44**, 3510 (2019).
[47] V. Karanikolas, I. Thanopulos, and E. Paspalakis, Phys. Rev. Research **2**, 033141 (2020).
[48] H. T. Dung, L. Knoll, and D.-G. Welsch, Phys. Rev. A **57**, 3931 (1998).
[49] H. T. Dung, L. Knoll, and D.-G. Welsch, Phys. Rev. A **62**, 053804 (2000).
[50] H. T. Dung, L. Knoll, and D.-G. Welsch, Phys. Rev. A **64**, 013804 (2001).
[51] S. Scheel and S. Y. Buhmann, Acta Physica Slov. **58**, 675 (2008).
[52] C. Van Vlack, P. T. Kristensen, and S. Hughes, Phys. Rev. B **85**, 075303 (2012).
[53] J. Hakami, L. Wang, and M. S. Zubairy, Phys. Rev. A **89**, 053835 (2014).
[54] Y.-W. Lu, L.-Y. Li, and J.-F. Liu, Sci. Rep. **8**, 7115 (2018).
[55] R. Geick, C. H. Perry, and G. Rupprecht, Phys. Rev. **146**, 543 (1966).
[56] Y. Guo, W. Newman, C. L. Cortes, and Z. Jacob, Adv. OptoElect. **2012**, 452502 (2012).
[57] J. A. Dionne, L. A. Sweatlock, H. A. Atwater, and A. Polman, Phys. Rev. B **72**, 075405 (2005).
[58] C. Sirtori, F. Capasso, J. Faist, and S. Scandolo, Phys. Rev. B **50**, 8663 (1994).
[59] J. H. Smet, C. G. Fonstad, and Q. Hu, J. Appl. Phys. **79**, 9305 (1996).
[60] Y. Li, H. Yan, D. B. Farmer, X. Meng, W. Zhu, R. M. Osgood, T. F. Heinz, and P. Avouris, Nano Lett. **14**, 1573 (2014).
[61] D. Rodrigo, O. Limaj, D. Janner, D. Etezadi, F. J. Garcia de Abajo, V. Pruneri, and H. Altug, Science **349**, 165 (2015).